Environmental Science Nano

ROYAL SOCIETY OF CHEMISTRY

PAPER

View Article Online
View Journal | View Issue

Cite this: *Environ. Sci.: Nano*, 2026, **13**, 1910

Possibilities and limitations of AFM-IR to detect nanoplastic particles in the atmosphere

Nico Kummer, *[a] Stefan Horender,[b] Tero S. Kulmala,[c] Konstantina Vasilatou,[b] Christoph Hueglin [d] and Ralf Kaegi *[a]

Potential impacts of nanoplastic particles (NPs) on human health through cellular uptake following inhalation have raised increasing concern. However, detection and quantification of atmospheric NPs remain challenging because most analytical methods lack either the spatial resolution or the chemical specificity needed to identify NPs in complex matrices. In this work, we investigate the possibilities and limitations of nanoscale infrared spectroscopy enabled by atomic force microscopy detection (AFM-IR) to identify NPs in ambient air. We establish an analytical framework that combines electrostatic precipitation, for representative nanoparticle collection on suitable substrates, with AFM-IR for chemical identification of individual particles at high spatial resolution. We achieved detection limits of 20 nm for silica and 80 nm for polystyrene nanoparticles. Experiments conducted with synthetic aerosols confirm that NPs can be distinguished from major atmospheric particle types including soot, mineral dust and sulfate salts. Ambient aerosol samples were dominated by sulfate, elemental and organic carbon with minor amounts of mineral dust. Statistical considerations based on the absence of NPs in atmospheric samples suggest that NPs are several orders of magnitudes less abundant than other particles in ambient air. The AFM-IR method offers nanoscale chemical information of NPs, which will be essential for characterizing urgently needed nanoplastic reference materials. Although the method allows distinguishing between major particle types present of ambient aerosols and is specific enough to unambiguously identify NPs, the limited throughput of the method will require a selective enrichment of NPs to confirm their presence in the atmosphere or in any other environmental compartment.

Received 10th December 2025,
Accepted 20th February 2026

DOI: 10.1039/d5en01155h

rsc.li/es-nano

Environmental significance

Airborne nanoplastic particles (NPs) are of increasing health concern. However, detection and quantification of NPs in complex matrices require both, high spatial resolution and chemical specificity. Atomic force microscopy (AFM) combined with infrared spectroscopy (IR) is an emerging technique fulfilling these requirements. In this paper, we develop a workflow including electrostatic deposition of airborne NPs on laser-cut silicon wafers, which are suitable for AFM-IR analysis. NPs spiked to synthetic aerosols, consisting of sulfate droplets, aged soot and mineral dust were successfully detected. Ambient aerosols were dominated by soot and sulfate droplets, but NPs were not detected. A statistical analysis suggested that nanoplastic particles are at least 2–3 orders of magnitudes less abundant than other particles found in ambient air.

1. Introduction

Plastic particles of diverse sizes are ubiquitous in the environment, and they have been found even in remote areas such as the Arctic, the deep sea and in the air we breathe, the water we drink and the food we eat.[1,2] Microplastic particles (<5 mm, MPs) and nanoplastic particles (<1000 nm, NPs) are classified as primary particles (*e.g.* intentionally added to cosmetics and paints) or secondary particles, which are generated from larger plastic objects through mechanical and chemical weathering in the environment.[1,3,4] Particles in the micrometer size range likely dominate the plastic mass, but NPs may dominate the number of plastic particles in the environment,[2] although experimental data on environmental occurrence of nanoplastic particles are still scarce. Wind and sea spray can transport NPs from soil and water to the atmosphere, where they age and mix with

[a] *Particle Laboratory, Department of Process Engineering, Eawag (Swiss Federal Institute of Aquatic Science and Technology), Ueberlandstrasse 133, 8600 Dübendorf, Switzerland. E-mail: n.kummer@hotmail.com, ralf.kaegi@eawag.ch*
[b] *Particles and Aerosols Laboratory, Federal Institute of Metrology METAS, Lindenweg 50, 3003 Bern, Switzerland*
[c] *Laboratory for Transport at Nanoscale Interfaces, Empa (Swiss Federal Laboratories for Materials Science and Technology), Ueberlandstrasse 129, 8600 Dübendorf, Switzerland*
[d] *Laboratory for Air Pollution and Environmental Technology, Empa (Swiss Federal Laboratories for Materials Science and Technology), Ueberlandstrasse 129, 8600 Dübendorf, Switzerland*

other natural (mineral dust, volcanic ashes, organic aerosols from plants) and anthropogenic aerosols (soot, brake and tire wear particles).[3,5,6] Nanoplastic particles in the atmosphere may affect the formation of clouds by acting as condensation nuclei, and might thus influence the atmospheric radiation balance due to cloud albedo, precipitation and cloud lifetime.[7] Through long-range atmospheric transport NPs are spread over the entire planet.[8] Due to their small size, NPs can penetrate cell membranes, enter cells, the blood stream and cross biological barriers (blood–brain, placental).[2] Recent reports suggest that NPs cause inflammation, DNA damage and cytotoxicity, leading to the development of cancer, metabolic disorders and neurodegeneration (dementia).[2,3,9,10] Furthermore, the release of carcinogenic and endocrine-disruptive additives increases the health risk of NPs.[9]

The current knowledge about plastic particles in the environment is largely based on studies addressing macro- and microplastics particles. The NP fraction, however, remains largely unexplored due to analytical challenges and issues related to sample collection.[1,11–13] Harmonized sampling protocols and many different analytical approaches have been suggested for microplastic particles, defined as plastic particles sized 5 mm–1 μm.[1,14] However, available sampling procedures rarely address NPs. The same trend becomes obvious when evaluating analytical techniques used for plastic detection. Macroplastic particles are visually identified and occasionally confirmed using spectroscopic methods (mainly Fourier transform-infrared (FT-IR) spectroscopy). For the identification of microplastics, two major approaches can be distinguished: (i) mass based methods, currently dominated by pyrolysis gas chromatography mass spectrometry (Py-GC-MS),[15] with results expressed in mass per volume or mass of environmental matrix, and (ii) number based methods, mostly based on (FT-)IR and Raman spectroscopy,[12,13] providing information about the number, size and shape of particles, along with their chemical identity. While the mass-based approach includes the NP fraction (although several sample preparation protocols include filtration steps where NPs are lost), the particle-based methods (dominated by infrared and Raman microspectroscopy) are diffraction limited with a resolution limit of around ~10 μm for μ-FT-IR,[13] and ~500 nm for both Raman[12] and optical photothermal infrared spectroscopy (O-PTIR).[13] Similar method detection limits were also reported from novel approaches using automated scanning electron microscopy in combination with energy dispersive X-ray analysis.[16]

Recently, several approaches based on atomic force microscopy (AFM) have been explored to overcome the diffraction limitation. Chemical maps or IR maps, referring to the spatial acquisition of the IR absorption at a fixed wavelength, can be recorded using photothermal infrared AFM (AFM-IR) in various measurement modes and scattering scanning near field optical microscopy (s-SNOM and derived nano-FTIR). Using these techniques, polymer particles <100 nm were successfully imaged.[17–20] In AFM-IR the expansion of the sample due to the photothermal effect, induced by the absorption of the IR laser, is detected.[21,22] If the IR laser is kept at a constant wavenumber while scanning with the probe and detecting the photothermal expansion, an IR absorption map is generated. If the probe is kept at a point of interest and the wavenumber of the IR laser is modulated, an IR absorption spectrum can be recorded.

First measurements of micro- and nanoplastics using AFM-IR and related techniques were published around 2020 and the data have recently been summarized.[13,23] Amongst others, the photooxidation of model microplastic particles, namely polyethylene (PE) and polystyrene (PS), and their interaction with fulvic acid have been explored using AFM-IR.[24–27] Furthermore, PS particles were detected in spiked Quagga mussels[28] using AFM-IR and PS nanoparticles (20–400 nm) mixed with salt (NaCl) water and hydrogen peroxide were identified in salt deposits using photoinduced force microscopy.[29] In addition to PS particles, polymethyl methacrylate (PMMA) and PE nanoparticles (200 nm) as well as a degraded polylactic acid (PLA) from coffee cup lids were identified in experimental studies using nano-FTIR.[30] Li and co-workers performed pioneering AFM-IR measurements of NPs in tap water and in water from a drinking water treatment plant.[31,32] While the AFM-IR data were only qualitative, results from Py-GC-MS measurements indicated the presence of PE, PS, polyvinyl chloride (PVC) resulting in a total NP concentration of 1.67–2.08 μg L^{-1} in tap water.[31] A combination of fluorescence microscopy and AFM-IR has been used to study the occurrence of NPs in bottled drinking water.[33] AFM-IR has further been used to analyze aerosol particles collected on impactor plates. These studies have focused on pharmaceutical aerosols,[34,35] synthetic atmospheric aerosols containing succinic acid, ammonium sulfate, sodium nitrate, sucrose, and polyethylene glycol[36] and ambient indoor aerosols, in which soot and proteinaceous particles have been identified.[37]

This brief literature review suggests that AFM-IR and related techniques are suitable for detecting NPs. However, sample preparation protocols suitable for AFM-IR measurements have not been established, yet. Although AFM-IR seems a promising approach for NPs detection in aerosol samples, well-characterized (reference) samples containing relevant components of ambient aerosols, are essential for determining the analytical performance of the AFM-IR method but are currently unavailable. As a result, atmospheric samples have not yet been systematically investigated, and existing AFM-IR studies remain largely qualitative and descriptive. The objectives of this study were therefore to (i) evaluate the most suitable substrate for NP analysis using AFM-IR, (ii) determine key analytical figures of merit, including size detection limits, specificity, and dynamic range for identifying NPs within mixed particle populations, and (iii) develop and validate an approach for

atmospheric aerosol sampling and subsequent AFM-IR analysis.

2. Experimental section

2.1. Model particle suspensions

The following NPs were purchased: PS nanospheres (diameters: 20, 50, 80, 200 nm, Thermo Scientific, CA, USA), silica nanospheres (diameters 20, 50, 80 and 200 nm, nanoComposix, CA, USA), PMMA nanospheres (diameter 100 nm, microparticles GmbH, Germany) and PE particles (200–9900 nm, Cospheric, CA, USA). Stock suspensions were prepared by diluting the PS, silica and PMMA particle suspensions to 0.1 mg mL^{-1} in ultrapure water (Arius Pro, Sartorius, Göttingen, 146 Germany). An initial PE suspension was prepared by mixing the polydisperse PE powder into 5 mL isopropanol (purity >99.8%, VWR International GmbH, Dietikon, Switzerland) at a concentration of 10 mg mL^{-1}. To remove larger PE particles, the suspension was sedimented overnight in a glass vial (infochroma ag, Switzerland) and, thereafter, 500 µL of supernatant were withdrawn. All stock suspension

Table 1 List of experimental particle suspensions. The mass of an individual particle was calculated based on the respective density (ρ) and the particle diameter (d). Dividing the mass concentration (c_m) by the mass of a single particle resulted in the calculated number concentration (c_n) of the respective suspension or aerosol. For the polymodal suspensions, the particle ratios were calculated by normalizing the number concentration to the least abundant particle type in the suspensions. PS: polystyrene, PE: polyethylene, PMMA: poly (methyl methacrylate)

Sample	Material	d^a (nm)	ρ (g cm^{-3})	c_m (mg mL^{-1})	c_n (n mL^{-1})	Ratio
Monomodal, monotype suspensions						
1	PS	20	1.05	0.01	2.27×10^{12}	
2	PS	50	1.05	0.1	1.46×10^{12}	
3	PS	80	1.05	0.1	3.55×10^{11}	
4	PS	200	1.05	0.1	2.27×10^{10}	
5	Silica	20	2.65	0.01	9.01×10^{11}	
6	Silica	50	2.65	0.1	5.77×10^{11}	
7	Silica	80	2.65	0.1	1.41×10^{11}	
8	Silica	200	2.65	0.1	9.01×10^{9}	
9	PMMA	100	1.18	0.1	1.62×10^{11}	
10	PE[b]	200	0.95	NA	NA	
Polymodal, monotype suspensions[c]						
11	Silica	20	2.65	0.025	2.25×10^{11}	1000
		50	2.65	0.025	1.44×10^{11}	64
		80	2.65	0.025	3.52×10^{10}	16
		200	2.65	0.025	2.25×10^{9}	1
Polymodal, polytype suspensions						
12	Sample 11	20–200	2.65	0.1	2.43×10^{12}	1527
	PS	80	1.05	0.001	3.55×10^{9}	2
	PMMA	100	1.18	0.001	1.62×10^{9}	1
Synthetic aerosols						
13	PS	200			3200	1
	Soot	180			8000	2.5
14	PS	200			3000	1
	Mineral dust	50			7000	2.3
15	PS	200			2500	1
	Nitrate/sulfate	136			7000	2.8
16	PS	200			700	1
	Soot	180			14 000	20
	Mineral dust	50			1000	1.4
	Nitrate/sulfate	136			1000	1.4
Ambient air						
17[d]	Ambient air	NA			NA	
	PS	200			2300	
18[e]	Ambient air	NA			NA	

NA: not available. [a] Diameter corresponds to nominal geometric diameter as declared by the manufacturer for model particle suspensions and to number-based geometric mean mobility diameter (GMDmob) measured for synthetic aerosols. [b] Supernatant of a suspension of polydisperse PE particles in isopropanol following overnight sedimentation (particle concentration in the supernatant was not determined). The size (200 nm) refers to the smallest particle diameter detected by atomic force microscopy (AFM) analysis. [c] Total: c = 0.1 mg mL^{-1}, 2.43×10^{12} n mL^{-1}. [d] Collected for 8 h on 19 August 2025. [e] Collected for 4 h on 19 June 2025.

and mixtures thereof were stored in glass vials (5 mL) that were previously cleaned with isopropanol.

Nanoparticle mixtures were prepared by diluting and mixing respective amounts of stock suspensions (Table 1). Number concentrations c_n were derived from the mass concentrations (c_m) of the respective stock suspensions using the following equation:

$$c_n = \frac{c_m}{\rho \frac{\pi}{6} d^3}$$

with ρ referring to the material density and d to the diameter of the particle. Number ratios were calculated by normalizing the number concentration to the least abundant particle type in the mixture.

2.2. Substrates for AFM-IR measurements

The following substates were evaluated for their suitability of AFM-IR measurements: Mica (10 mm diameter, micro to nano, The Netherlands), silicon (Si)-wafers (undoped, native oxide layer, 525 μm thickness, diced into 5 × 5 mm squares, Micro to Nano) and transmission electron microscopy (TEM) grids (carbon coated Cu grids, 200 nm mesh, EMResolutions, UK). To test plasmonic signal enhancement as described in literature,[38] 20 nm gold was sputter-coated onto the freshly cleaved mica substrate using an EM ACE600 sputter coater (Leica Microsystems GmbH, Wetzlar, Germany). Additionally, laser-cut silicon octagons (d ~3 mm, 525 μm thick, undoped, with a native oxide layer) were fitted into the electrostatic precipitator (PartectorTEM, naneos particle solutions GmbH, Switzerland). and used for aerosol sampling. The details on their fabrication are given in the SI Method M1.

2.3. Deposition of nanoparticles from suspensions on AFM substrates

Nanoparticles were deposited onto individual AFM substrates using piston pipettes with polypropylene pipette tips (Table 1). A volume of 5 μL was spread out on the AFM substrates and dried under a gentle air stream. As the working suspensions had high particle concentrations (Table 1) and the AFM-IR method is rather insensitive to the presence of minor amounts or particles resulting from potential contamination, we have decided to proceed without preparing blind samples (*e.g.* filtered DI water).

2.4. Synthetic aerosol

Synthetic aerosols mimicking ambient airborne particles were generated in the experimental facility for production of ambient-like model aerosols (PALMA) at the Federal Institute of Metrology, METAS.[39] The synthetic aerosol consisted of inorganic salt nebulized from solutions of ammonium nitrate (>99%, Acros Organics, Slovakia) and ammonium sulfate (>99.5%, Acros Organics; Netherlands), mineral dust particles (ISO A2 test dust, 72% SiO_2, DMT, USA) dispersed by a rotating-brush generator, soot photochemically aged by ozonolysis of α-pinene (>97%, Sigma Aldrich, Switzerland) generated in a prototype micro smog chamber,[40] and 200 nm PS particles (microparticles GmbH, Germany). The generated particles were fed into the PALMA facility, operated with a constant flow of 60 L min^{-1}, at 21 °C and relative humidity of 40%. The aerosol was generated according to a previous protocol,[41] with minor differences and equipment specified in the SI, Method M2 and Fig. S1–S5. Aerosol collection was achieved through electrostatic precipitation (PartectorTEM, naneos particle solutions GmbH, Switzerland). For that purpose, the PartectorTEM was connected to the isokinetic sampling ports, and the mixed synthetic aerosols (samples 13–16) were sampled at a flow rate of 0.5 L min^{-1} and directly deposited onto the laser-cut Si-wafer octagons. Despite the predicted dependencies of the charging and consequently deposition efficiencies on the dielectric properties of the materials, experimental results obtained from silver and sodium chloride (nano) particles (showing very different dielectric constants) were identical considering the analytical uncertainties.[42,43] We, thus, assumed that the deposition efficiencies of the different particle types investigated in this study were independent of their material properties. The details about the PartectorTEM are described in a previous report.[43] The background concentration of the nanoparticles in the laboratory was also measured using the PartectorTEM. The average concentration values were mostly at or below 1 μm^2 cm^{-3} (lung deposited surface area, LDSA), which was several orders of magnitudes lower compared to the concentration values recorded during the synthetic aerosol sampling campaigns. We, therefore, considered the (nano) particulate contamination resulting from the atmospheric deposition in the laboratory as negligible.

2.5. Ambient aerosol

Ambient aerosols were also collected using the PartectorTEM. An ambient aerosol sample was collected for 4 hours on 19 June 2025 June (Table 1, sample 18) and a second sample (Table 1, sample 17) was collected for 8 h on 19 August 2025. For sample 17, we electrostatically deposited PS particles (200 nm) from a synthetic aerosol on the laser-cut silicon octagon prior to ambient air sampling. Sample 17 is therefore referred to as spiked environmental sample. For aerosol collection, the PartectorTEM was placed next to other measurement devices from the Swiss national air pollution monitoring network (NABEL) in Dübendorf. The PartectorTEM collects particles with diameters ranging from ~10 nm to 10 μm in diameter with a deposition efficiency (normalized to the TEM grid) of ~1–2% and with a flow rate of 0.5 L min^{-1}.[43]

2.6. Infrared atomic force microscopy (AFM-IR)

For the analysis of the samples deposited on the various AFM substrates, a NanoIR 2 AFM-IR system (Anasys/Bruker, USA) in combination with PR-EX-TnIR-A tapping mode probes (Bruker, USA; 75 kHz resonance frequency, spring constant

1–7 Nm^{-1}, gold coating, tip nominal radius 20 nm) was used. As tapping AFM-IR mode offered gentle imaging of particles, and imaging in contact mode led to immediate removal of particles and tip contamination, we operated the instrument in tapping mode. The tapping mode AFM-IR measurements were performed at a scan rate of 1 Hz and at 256 × 256 pixels, resulting in scan times of 4 min and 16 s per frame. Chemical images (IR maps) were recorded at fixed wavenumbers and helped to detect the particles of interest. AFM-IR spectra were obtained on individual particles of interest by sweeping the entire wavenumber range of the quantum-cascade laser (950–1948 cm^{-1}) at various laser powers (depending on the polymer and signal from the vibrational band). The presented spectra were acquired at a spectral resolution of 2 cm^{-1} and represent at least three consecutive scans that were automatically averaged by the Analysis Studio software which, was used to operate the instrument. Three consecutive scans were selected as a compromise between improving signal to noise ratio and increasing measurement times. All AFM-IR measurements were conducted under ambient conditions (23 °C, 20% relative humidity), without using nitrogen purging. The recorded images and spectra were exported from the Analysis Studio software for further processing. Height images were flattened with the Gwyddion software (0th to 2nd order flattening). The recorded spectra were processed using an in-house Python script to eliminate offsets at the laser chip transitions, to remove spikes (adjacent averaging) and to apply Savitzky–Golay smoothing filter with a 2nd order window of 7 points. For better visual comparison, all spectra were normalized to an intensity of 1, and the *y*-axis was expressed in arbitrary units (a.u.).

2.7. Atomic force microscopy

Additional AFM measurements were conducted using a Dimension Icon (Bruker, USA) operated in ScanAsyst mode (force-controlled) with ScanAsyst-Air probes (tip nominal radius 2 nm). Raw images were flattened with the Gwyddion software.

2.8. Attenuated total reflectance Fourier-transform infrared spectroscopy (ATR-FTIR)

Attenuated total reflectance Fourier transform infrared spectroscopy (ATR-FTIR) measurements were conducted on a Tensor-27 spectrometer (Bruker, USA). After recording background spectra, a drop of the polymer particle stock suspensions was dried on the ATR crystal using a heat gun. The spectra were recorded at a resolution of 4 cm^{-1} and included 32 scans.

2.9. Scanning electron microscopy with energy-dispersive X-ray spectroscopy (SEM–EDX)

For imaging, the scanning electron microscope (Gemini 460, ZEISS, Germany) was operated at acceleration voltages of 3 kV and a current of 72 pA. For image formation, a secondary electron detector (either InLense or Everhard Thornley type) was used. For elemental analysis of selected particles, the SEM was operated at an acceleration voltage of 5 kV and a current of 500 pA. Individual elemental spectra were recorded using an energy dispersive X-ray (EDX) analysis system (Ultim MAX 170 mm detector, Oxford instruments, UK) coupled to the microscope. Spectral processing was done using the software code AZTEC (Oxford Inst, UK). For SEM measurements, samples were coated with 5 nm of carbon using a CCU-010 carbon coater (safematic, Zizers, Switzerland).

3. Results & discussion

The identification of individual NPs requires (i) high spatial resolution to detect individual nanoparticles and (ii) sufficient chemical specificity to distinguish between different polymer types. Atomic force microscopy–infrared spectroscopy (AFM-IR) combines the nanoscale spatial resolution of AFM with the chemical specificity of IR spectroscopy.[44] This technique should be particularly well-suited for NP analysis due to the high thermal expansion coefficient of polymers, which enables infrared spectroscopy through the detection of photothermal expansion using an AFM cantilever. However, before AFM-IR can be reliably applied to atmospheric or environmental samples in general, methodological challenges need to be systematically assessed. These include the evaluation of optimal AFM-IR substrates and the characterization of key performance parameters, such as the size limit of detection, specificity for different chemical composition, and the dynamic range for identifying NP within mixed particle populations.

3.1. Substrate evaluation for AFM-IR measurements of nanoplastic

The choice of the substrate is critical for the quality AFM measurements in general, but even more so for AFM-IR, because the IR response of the substrate can introduce unwanted background absorption or, conversely, plasmonic enhancement of the photothermal effect on which the IR signal detection is based. We evaluated the following 4 substates, which, based on literature data were most promising: i) Si-wafer, ii) pristine mica, iii) mica sputter-coated with a 20 nm gold layer and iv) copper TEM grids with a carbon film. On each of the substrates 80 nm PS particles were drop-casted. Chemical imaging at a fixed wavenumber, as well as full spectral acquisition of individual particles and the substrate were conducted. Before each measurement, a cantilever tune was conducted for the first resonance mode, and the tune of the second resonance mode for IR detection was performed on top of a PS particle at a laser wavenumber of 1492 cm^{-1}. The laser power IR imaging was set to 100%, which was sufficient to induce detectable photothermal expansion of the material without thermally degrading it. Quaroni (2020)[45] reported AFM-IR measurements using laser powers of ~1–3 mW and IR spot diameters of ~100–200 μm

with the same Anasys NanoIR2 AFM-IR equipped with a MIRcat laser, as we used for our experiments. Based on the data presented by,[45] we expect that laser powers per unit area were between 30–400 mW mm^{-2} in our experiments.

The Si-wafer proved most suitable for both topographic and chemical imaging as well as for the acquisition of full AFM-IR spectra from individual 80 nm PS particles (Fig. 1A). The AFM-IR spectrum obtained on a PS particle displayed characteristic absorption bands at 1028 cm^{-1} (aromatic CH bend), 1452 cm^{-1} (CH_2 bend), 1492 cm^{-1} (aromatic ring stretch), and at 1600 cm^{-1} (aromatic ring stretch), in good agreement with data from ATR-FTIR measurements (Fig. S6A) and the literature.[46] Measurements of the pristine Si-wafers showed peaks related to the native silicon oxide layer (Fig. 1A). The main peaks were related to Si–O stretching vibration at 1100 cm^{-1} and the longitudinal optical (LO) phonon at 1250 cm^{-1}.[47] Otherwise, limited contribution from the substrate to the IR spectra were observed. Also, the other substrates investigated in this study provided clean and flat surfaces that were adequate for morphological imaging of the deposited particles but were less suitable for spectral acquisitions. Individual PS particles were successfully located on both pristine and gold-coated mica substrates based on chemical maps recorded at 1492 cm^{-1} (Fig. 1B and C). However, recording full AFM-IR spectra of individual PS particles was impossible. Similar observations have also been reported in the literature and have been explained by an insufficient photothermal and mechanical coupling between the AFM tip and the material, which however still allowed recording (qualitative) chemical maps.[38,44] For the carbon-coated copper TEM grid, the strong IR absorption of the carbon film relative to the PS particles led to an inverted IR

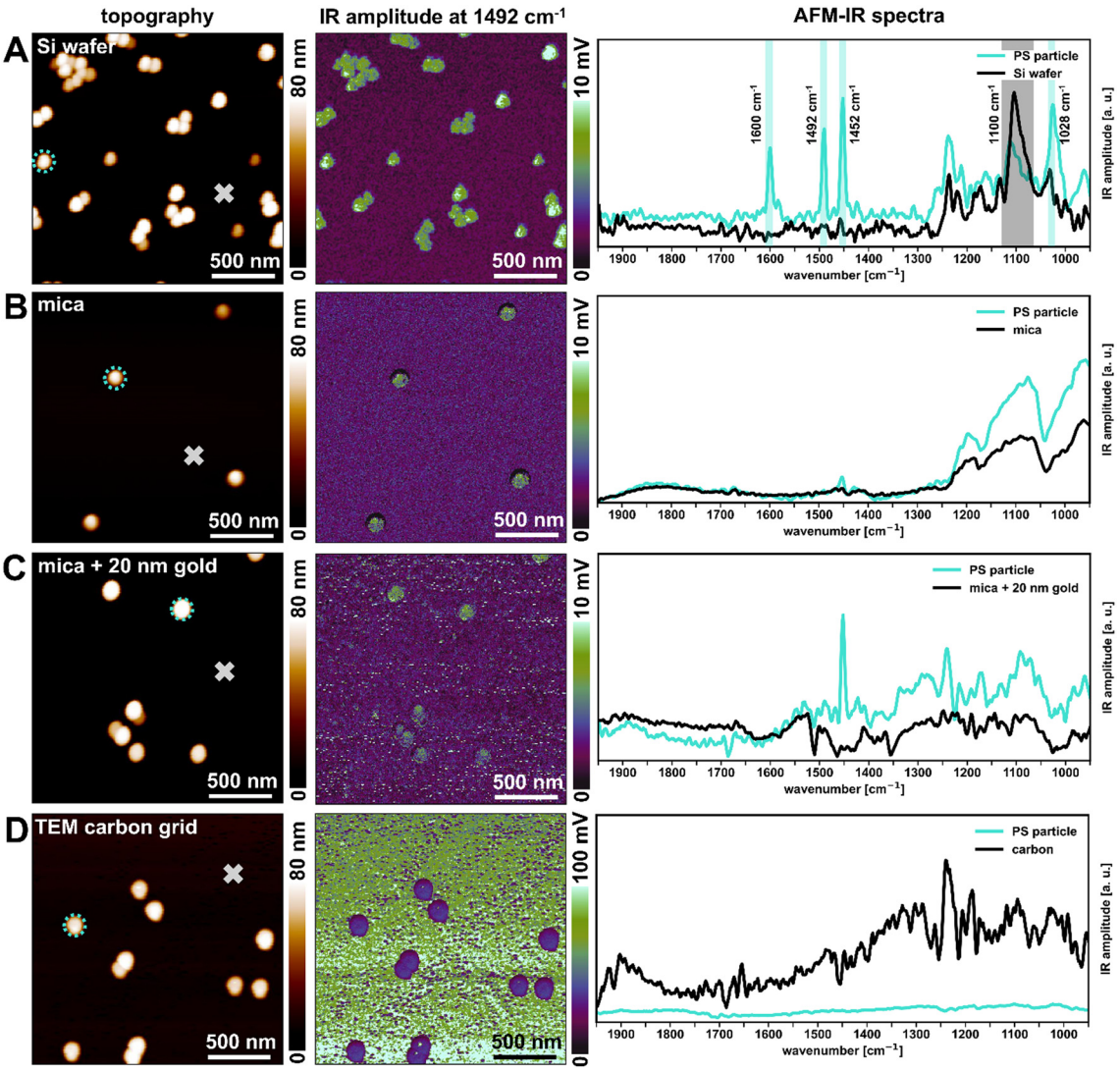

Fig. 1 Atomic force microscopy-infrared spectroscopy (AFM-IR) topography (left column), IR amplitude images at 1492 cm^{-1} (C=C stretching vibration of polystyrene (PS) phenyl group) (middle column) and spectra of 80 nm PS particles (sample 3) deposited on different substrates (right column): (A) Si-wafer, (B) mica, (C) mica coated with 20 nm gold, and (D) carbon transmission electron microscopy (TEM) grid. The spectra were recorded in the center of PS particles (dashed circle) and on the substrates (cross).

contrast in the amplitude image (Fig. 1D), consistent with the pronounced IR spectra recorded from the carbon film. Our results are, thus, in good agreement with previous reports[36,38] and we selected Si-wafers for subsequent investigations.

3.2. Particle specific size detection limits

The smallest particles that can be detected by AFM-IR differ among polymers because the IR absorption signal depends on polymer properties such as the strength of the vibrational dipole moments and the thermal expansion. As a result, the detection limit must be determined individually for each (polymer) type. In this study, the size detection limits were evaluated for PS (20, 50, 80, and 200 nm, prepared according to Table 1, samples 1–4) and silica nanoparticles (20, 50, 80, and 200 nm, prepared according to Table 1, samples 5–8) deposited on Si-wafers. For PMMA (100 nm, Table 1, sample 9) and PE (200 nm, Table 1, sample 10), measurements were performed using the smallest commercially available particles. All measurements were conducted using the operational conditions established in the previous section. The laser power was reduced whenever the signal intensity permitted this.

Topographic measurements of PS particles with diameters of 200 and 80 nm were in good agreement with the nominal particle diameters (Fig. 2A and B, height profiles provided in Fig. S7). Polystyrene particles of these sizes were also correctly identified in the chemical maps recorded at 1492 cm^{-1}. Furthermore, characteristic AFM-IR spectra were

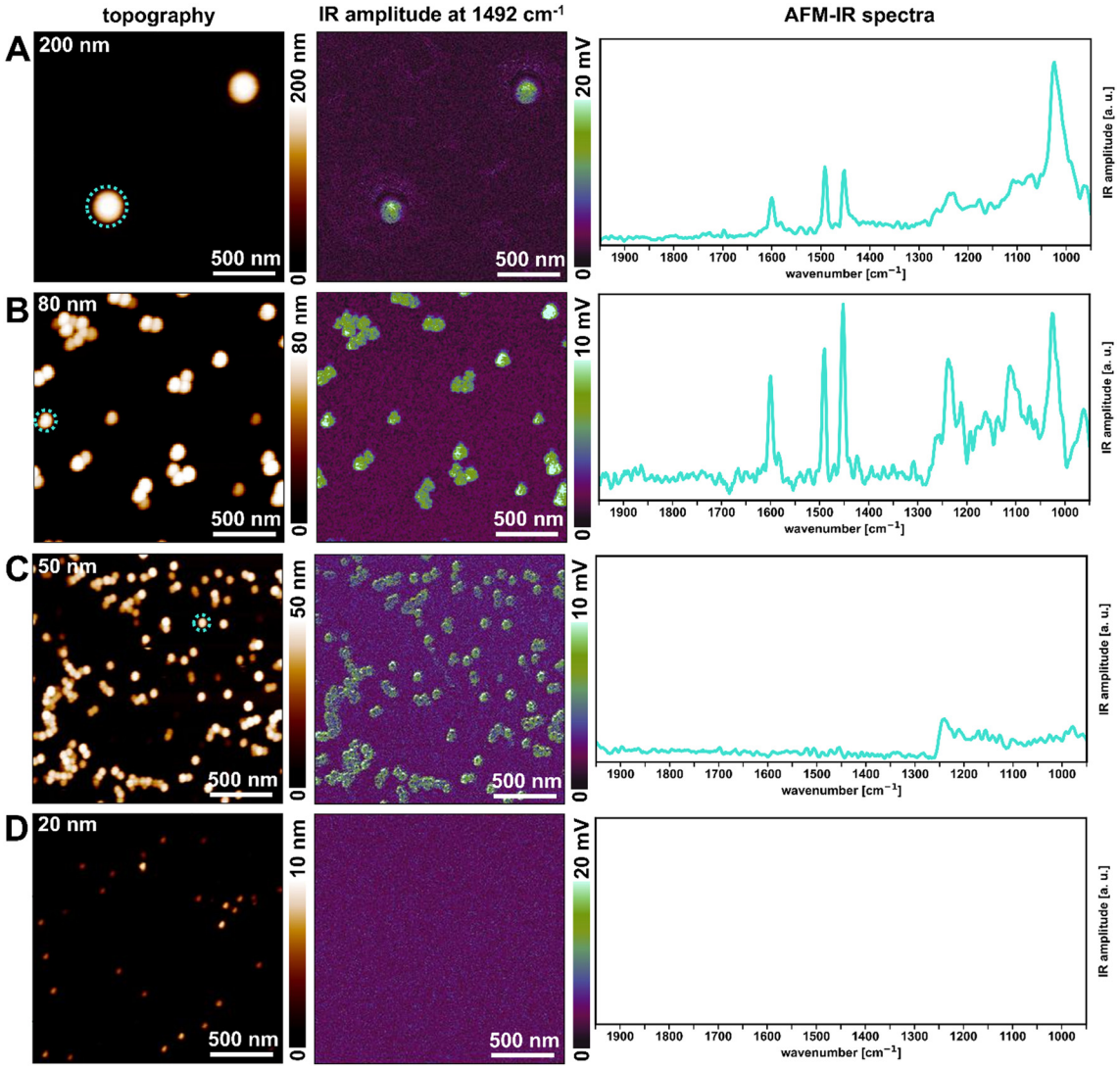

Fig. 2 Atomic force microscopy-infrared spectroscopy (AFM-IR) topography images (left column), IR amplitude images at 1492 cm^{-1} (C=C stretching vibration of polystyrene (PS) phenyl group) (middle column) and AFM-IR spectra of PS particles of different sizes deposited on Si-wafers (right column): (A) 200 nm, (B) 80 nm (data replotted from Fig. 1A for completeness), (C) 50 nm, and (D) 20 nm (samples 1–4, Table 1). The spectra were recorded from the center of the encircled PS particles. As particles could not be identified on the chemical maps, no attempts were made to record AFM-IR spectra (D). Relative intensities of individual peaks can vary due to the variability in the IR tune for the four quantum cascade laser stages of the AFM-IR instrument and due to spectral processing.

successfully recorded from individual PS particles of 200 nm and of 80 nm (Fig. 2A and B). In contrast, 50 nm PS particles were detectable in both topography and IR amplitude maps at 1492 cm^{-1}, but the recorded IR spectra from individual 50 nm PS particles were inconclusive (Fig. 2C). The maximum height of individual PS particles decreased from 45 nm (before analysis) to 17 nm (after acquiring full IR spectra, Fig. S8), indicating the degradation of the 50 nm PS particles due to the combined impacts of the laser beam (100% power) and the oscillating AFM tip. The 20 nm PS particles were clearly visible in the morphological AFM images; however, the maximum height was 10 nm and, thus, substantially smaller than the certified particle size (Fig. 2D and S9A). However, results from additional measurements performed with a conventional AFM (Bruker Dimension Icon) operated in force-controlled ScanAsyst mode agreed with the certified diameter (20 nm) of the particles (Fig. S9B). Furthermore, although individual 20 nm PS particles were observed in the topographic images, chemical maps recorded at 1492 cm^{-1} did not reveal the presence of any PS particles. This was most likely due to an insufficient signal-to-noise ratio. Thus, a reduction of the laser power was not attempted, as this would have further lowered the spectral quality (signal-to-noise ratio). As we were not able to localize the 20 nm PS particles based on the chemical maps (wavenumber fixed to 1492 cm^{-1}) no attempts were made to record full AFM-IR spectra. This observation suggests that the smallest PS particles rapidly degraded under the operational conditions used for AFM-IR measurements. Thus, the size detection limit for PS NPs allowing spectral confirmation was between 50 and 80 nm.

Silica particles (20–200 nm) drop-casted onto Si-wafers were unambiguously detected in topographic AFM images (Fig. S10, height profiles given in Fig. S11) and even the 20 nm silica particles were clearly identifiable in chemical maps recorded at 1100 cm^{-1}. Although the native oxide layer (expected thickness of 1–2 nm (ref. 48)) developed on the Si-wafer also absorbs IR radiation at this wavenumber, the IR absorption from the silica particles was more intense and provided sufficient IR contrast to localize individual particles (Fig. 3A). Full AFM-IR spectra were dominated by a single prominent peak at around 1100 cm^{-1}, corresponding to the Si–O stretching vibration (Fig. 3A and S10). As this prominent peak was observed in the AFM-IR spectra of all silica particles, their size detection limit was set to 20 nm, corresponding to the smallest particle size evaluated. It is possible that even smaller silica particles can be detected both spectroscopically and based on topographic images, however, such particles were not available in this study. PMMA particles were available at a nominal size of 100 nm and PE particles were extracted from a suspension made from polydisperse PE powder. The smallest PE, characterized

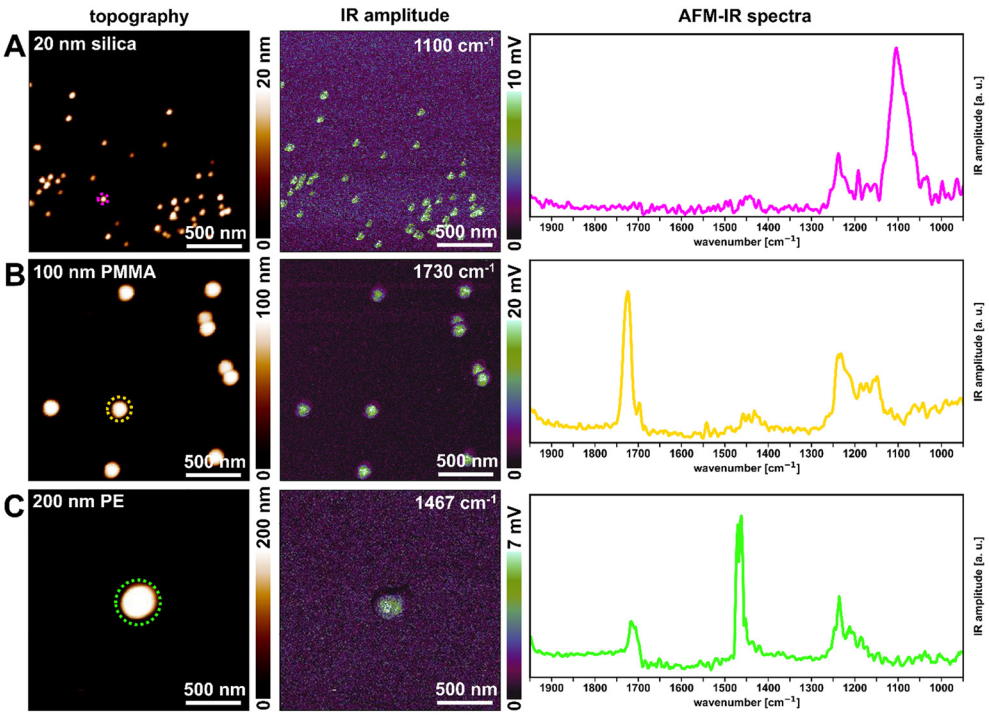

Fig. 3 Atomic force microscopy-infrared spectroscopy (AFM-IR) topography (left column), IR amplitude images at relevant wavenumbers (middle column) and spectra of the smallest particles available for each material deposited on Si-wafers (right column): (A) 20 nm silica (sample 5) detected in IR amplitude maps through peak at 1100 cm^{-1} (Si–O stretching vibration of silicates), (B) 100 nm poly(methyl methacrylate) (PMMA, sample 9) detected in IR amplitude maps through peak at 1730 cm^{-1} (C═O stretching vibration of ester group), (C) 200 nm polyethylene (PE, sample 10) detected in IR amplitude maps through peak at 1467 cm^{-1} (C–H bending vibration of methylene group). The spectra were recorded in the center of the encircled particles.

by SEM (Fig. S12) were as small as 200 nm corresponding well to the minimum size of the PE reported by the manufacturer. Individual PMMA and PE particles were successfully localized on topographic as well as on chemical images (Fig. 3B and C). The AFM-IR spectra of the PMMA particles displayed a strong absorption band at 1730 cm^{-1} (Fig. 3B), characteristic of the ester carbonyl stretching vibration and the spectra for the smallest PE particles (~200 nm) exhibited a distinct absorption peak at 1467 cm^{-1} (Fig. 3C), corresponding to the methylene C–H bending vibration. The AFM-IR spectra from all these different polymer types were very similar to the corresponding ATR-FTIR spectra recorded on the same materials(Fig. S6). For silica, PMMA and PE particles the reported detection limits corresponded to the smallest particle sizes that were commercially available. Therefore, the true instrumental detection limits for these particles may be even lower. However, the size detection limits obtained from this study are similar to the smallest particle sizes reported from contact mode AFM-IR measurements, namely 100 nm for PS, and 80 nm for PE, respectively.[33] Furthermore, a nano-FTIR study has reported IR mapping and spectroscopy on PMMA particles as small as 140 nm.[30] The particularly low detection limit of 20 nm for silica obtained in our study can be attributed to the strong Si–O dipole moment, which results in intense infrared absorption and efficient photothermal expansion. In contrast, PS particles are more challenging to detect because the IR absorption in PS originates from non- or less polar C–C and C–H bonds. Therefore, higher laser powers are required to reach sufficient signal intensities, which, however, also increases the risk of local heating and particle degradation during the measurements.

The upper size limit of the AFM-IR method is independent of the materials but only determined by the limitation of the piezoelectric actuator, which is usually between 1 and 10 µm. However, for the analysis of nano- or microplastic particles larger than ~500 nm, other techniques such as O-PTIR as described in the introduction may be more suitable. We, thus, recommend the AFM-IR technology for particles smaller than 500 nm.

3.3. Specificity and dynamic range

Polymer and silica nanoparticles were mixed and drop-casted onto Si-wafers to evaluate the material specificity of the AFM-IR method. To assess the dynamic range, a polydisperse silica mixture was prepared with calculated number ratios of 1000 : 64 : 16 : 1 for the 20, 50, 80, and 200 nm silica particles, respectively (sample 11). This mixture was subsequently combined with 80 nm PS and 100 nm PMMA particles, resulting in a number ratio of 1527 : 2 : 1 for silica : PS : PMMA particles (sample 12).

In the topographic AFM image of the silica-PS-PMMA mixture (sample 12), individual polymer particles are identical to the silica particles (Fig. 4A), demonstrating that additional spectroscopic information is required to unambiguously identify NPs. Therefore, a series of chemical maps were sequentially recorded at the following wavenumbers (Fig. 4B–D), which represented characteristic IR absorption bands of the different particle types: 1100 cm^{-1} for silica (Si–O stretching vibration), 1492 cm^{-1} for PS (C=C stretching vibration of the phenyl ring), and 1730 cm^{-1} for PMMA (C=O stretching vibration). Based on the chemical maps, particles of interest were localized, and AFM-IR spectra were recorded on selected particles of interest (Fig. 4E). The acquired spectra were similar to those recorded on the silica, PS, and PMMA particles (Fig. S6), confirming that individual polymer particles can be identified even in the presence of overwhelming amounts of silica particles of similar sizes.

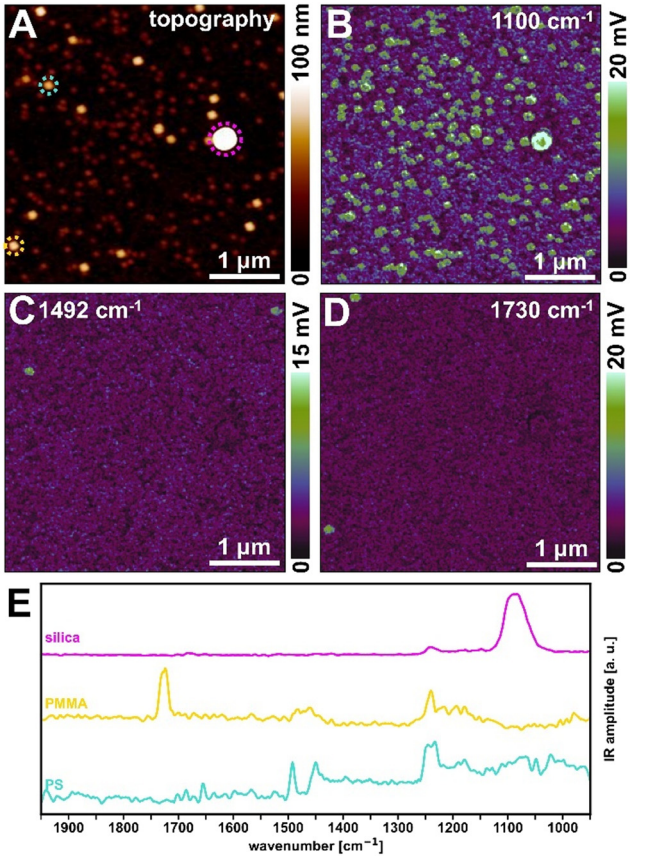

Fig. 4 Atomic force microscopy-infrared spectroscopy (AFM-IR) topography (A) and corresponding chemical images recorded at 1100, 1492 and 1730 cm^{-1} (B–D) of the nanoplastic (NP)-silica mixture consisting of polydisperse silica particles (20, 50, 80, 200 nm, 1000 : 64 : 16 : 1 number ratio, sample 11) used to dilute 80 nm polystyrene (PS) and 100 nm polymethyl methacrylate (PMMA) suspensions (sample 12, ratio of silica : PE : PMMA = 1527 : 2 : 1). The AFM-IR spectra (E) were recorded on the encircled particles. Magenta = silica, cyan = PS, yellow = PMMA.

3.4. Synthetic atmospheric aerosol

To mimic atmospheric aerosols, soot coated with oxidized products of α-pinene, mineral dust and inorganic salts (ammonium sulfate and nitrate), as well as 200 nm PS

particles as model NP were generated. The individual aerosol streams were combined, and a fraction of the mixed aerosol stream was electrostatically deposited on laser-cut Si-wafers using the PartectorTEM (Fig. S13). The samples (samples 13–16) were used to obtain characteristic topographic images and AFM-IR spectra of atmospherically relevant particles (Fig. 5) with different chemical composition. The particle number size distribution of the synthetic aerosol consisting of PS particles (200 nm), ammonium sulfate/nitrate, aged soot and mineral dust (sample 16) was reconstructed based on the AFM height profiles of individual particles and converted into the same units as the SMPS data, considering the investigated area, the sampled volume and the deposition efficiency of the PartectorTEM (Fig. S5). The good correspondence between the SMPS (Fig. S4) and the AFM-based particle size distribution (Fig. S5) confirmed that atmospheric particles were representatively collected by the PartectorTEM unit.

Aged soot: The broad and noisy absorption peak centered around 1580 cm^{-1}, dominating the AFM-IR spectra of individual soot particles can be attributed to C=C stretching vibrations within the conjugated graphitic domains of soot[49] and oxidized α-pinene (Fig. 5A, sample 13). The AFM-IR spectrum obtained on a PS particle displayed characteristic absorption bands at 1028 cm^{-1}, 1452 cm^{-1}, 1492 cm^{-1} and at 1600 cm^{-1}. Chemical images recorded at 1492 cm^{-1} showed both PS and soot particles. The absorption band at 1492 cm^{-1} is therefore not specific enough to distinguish between PS and soot particles. An additional chemical map was, therefore, recorded at 1580 cm^{-1} where only soot exhibited a strong absorption and consequently, only soot particles appeared on these additional chemical maps. The combination of the information from both chemical images eventually allowed distinguishing between soot and PS particles.

Mineral dust (sample 14) strongly absorbed IR radiation at a wavenumber of 1100 cm^{-1}, corresponding to the Si–O stretching vibration (Fig. 5B). Therefore, the chemical images recorded at 1492 cm^{-1} (specific for PS) and 1100 cm^{-1} (specific for mineral dust) enabled a clear distinction between PS and mineral dust particles.

Salt aerosols were produced by nebulizing a 1 : 1 (wt/wt) mixture of ammonium sulfate and ammonium nitrate (Fig. 5C, sample 15). The IR spectrum recorded on a salt particle was dominated by an absorption band at 1100 cm^{-1}, which is assigned to S–O stretching vibrations.[50] No additional bands attributable to ammonium or nitrate ions were observed, likely because part of the nitrate component

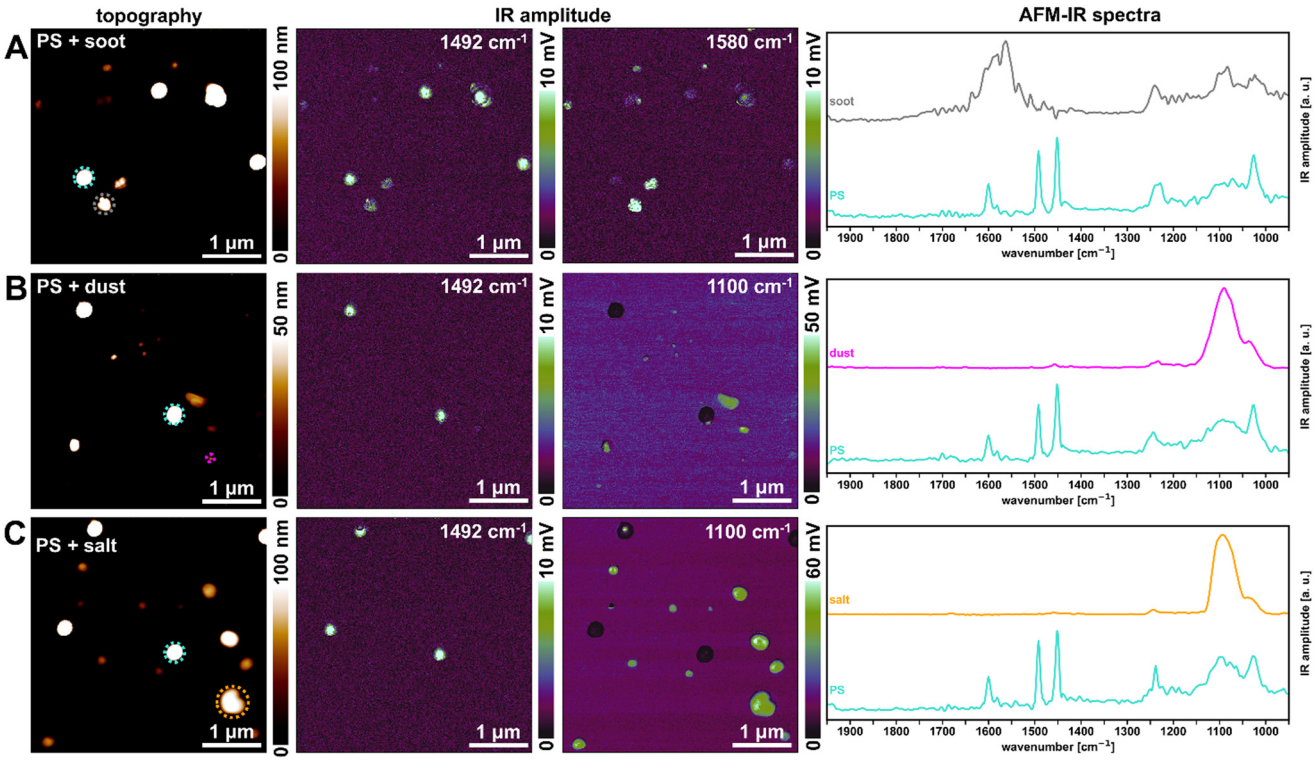

Fig. 5 Atomic force microscopy-infrared spectroscopy (AFM-IR) topography images (left column), chemical images at relevant wavenumbers (second and third columns from the left) and spectra of the individual, aerosol particles deposited onto Si-wafers using electrostatic precipitation (right column): (A) 200 nm polystyrene (PS) particles mixed with soot (sample 13), detected in IR amplitude maps through the absorption at 1492 cm^{-1} and 1580 cm^{-1} (C=C graphitic vibrations), respectively. (B) 200 nm PS particles mixed with mineral dust (sample 14) detected in IR amplitude maps through the absorption at 1492 cm^{-1} and 1100 cm^{-1} (Si–O stretch), respectively. (C) 200 nm PS particles mixed with ammonium sulfate/nitrate (sample 15), detected in IR amplitude maps through the absorption at 1492 cm^{-1} and 1100 cm^{-1} (S–O stretch), respectively. The spectra were recorded in the center of the encircled particles. The spectra of PS are always provided in cyan.

volatilized during aerosol generation, transport, or deposition. Salt particles consisting predominantly of sulfate were readily distinguished from PS in chemical maps recorded at 1100 cm^{-1} and 1492 cm^{-1}.

The synthetic aerosol mixture containing aged soot, mineral dust, and ammonium nitrate/sulfate, spiked with 200 nm PS particles (sample 16) was used to evaluate whether individual PS particles can be localized in the presence of other, relevant atmospheric particles based on specific chemical maps. For that purpose, topography (Fig. 6D) and chemical maps at the following three wavenumbers were sequentially acquired (Fig. 6A–C): 1100 cm^{-1}, indicative for sulfate and mineral dust (Si–O and S–O stretching vibrations), 1492 cm^{-1} indicative for PS (C═C stretching vibration of the phenyl ring; soot will also result in IR absorption at this wavenumber as noted above and thus additional spectral information is required to distinguish between PS and soot), and 1580 cm^{-1} indicative for soot (C═C vibrations of graphitic domains) (Fig. 6). The chemical map recorded at 1100 cm^{-1} was dominated by signals from sulfate particles. This was confirmed by AFM-IR spectra (Fig. 6E) recorded on respective particles showing a single strong absorption band at 1100 cm^{-1}. The IR map recorded at 1492 cm^{-1} revealed PS and soot particles, whereas only the latter ones were visible in chemical maps recorded at 1580 cm^{-1} (Fig. 6B and C).The results from these experiments demonstrated that the relevant components of ambient aerosols can be identified based on a suite of chemical images sequentially recorded at specific wavenumbers. Because both silicates and sulfate absorb near 1100 cm^{-1}, they were collectively classified as inorganic components.

Although the experiments using synthetic aerosols were only conducted using PS representing NPs, we assume that the results are also applicable to other polymer types, such as PE and PMMA. This is further supported by the position of the major absorption peaks of PMMA (~1730 cm^{-1}) and PE (~1450 cm^{-1}) which do not interfere with absorption bands of soot, dust or salts.

3.5. Ambient atmospheric aerosol

Building on the findings from the previous experiments, which demonstrated that synthetic aerosols collected by electrostatic precipitation (PartectorTEM) on Si-wafers can be distinguished through chemical mapping, ambient atmospheric aerosol samples were collected analogously at a suburban station of the Swiss National Air Pollution Monitoring Network (NABEL) in Dübendorf.

3.5.1. Measurements of untreated samples (spiked with PS). To confirm that NPs can be detected in the presence of ambient atmospheric particles, PS particles (200 nm) were deposited on a Si-wafer prior to using this Si-wafer for collecting an ambient aerosol sample (sample 17). Chemical images were recorded at 1100 cm^{-1} for sulfate and mineral dust, 1492 cm^{-1} for PS and soot, and 1580 cm^{-1} for soot-specific absorption (Fig. 7A–F).

Agglomerated soot and PS particles represented the largest features in respective AFM height image (Fig. 7G and S14). Individual salt and soot particles reached up to 100 nm, but were mostly smaller than that. Because of the pronounced topographic variations, phase contrast images sensitive to mechanical and adhesive properties provided additional contrast that helped to visualize particle boundaries (Fig. S14A). Furthermore, reducing the scanned size to 2 × 2 μm^2 decreased the tip velocity and improved spatial resolution, which enabled the detection of particles as small as 10 nm in

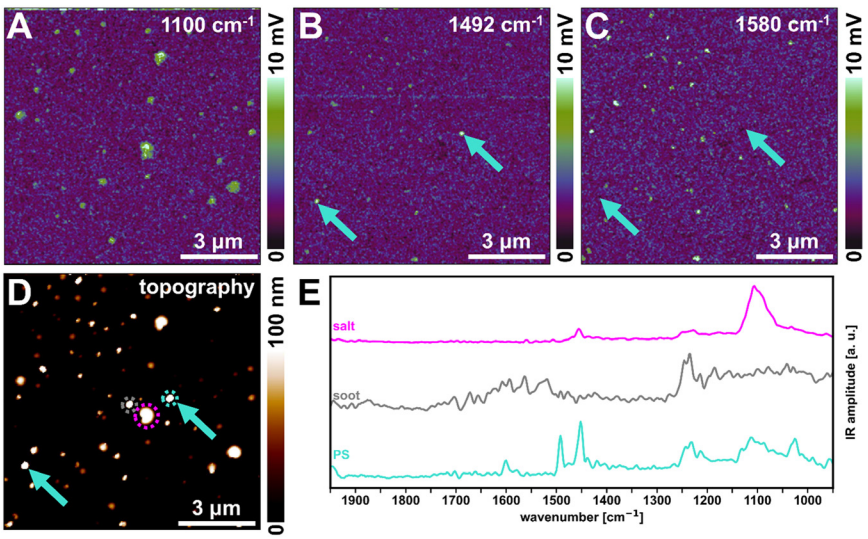

Fig. 6 Atomic force microscopy-infrared spectroscopy (AFM-IR) chemical maps recorded at 1100 cm^{-1}, 1492 cm^{-1} and 1580 cm^{-1} (A–C) of the synthetic aerosol consisting of aged soot, mineral dust, ammonium sulfate/nitrate salt and 200 nm polystyrene (PS) particles (sample 16). The identified PS particles are indicated by arrows in the corresponding topographic image (D). The AFM-IR spectra (E) were recorded on the particles encircled in color (magenta = salt, grey = soot, cyan = PS).

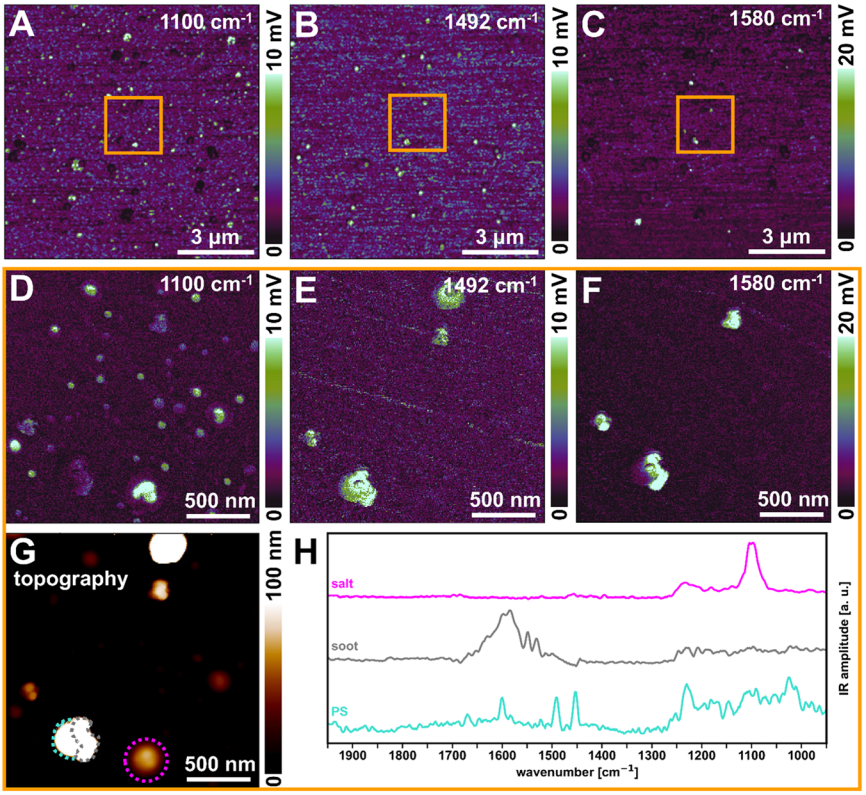

Fig. 7 Atomic force microscopy-infrared spectroscopy (AFM-IR) chemical images of the ambient aerosol deposited on Si-wafer previously spiked with 200 nm polystyrene (PS) particles (sample 17). (A and D) Chemical images at 1100 cm^{-1} to identify salt/dust particles, (B and E) 1492 cm^{-1} indicative for soot and PS and (C and F) 1580 cm^{-1} indicative for soot. (D–F) are detailed AFM-IR chemical images of the area indicated by the orange box in (A–C). The corresponding topography image (G) with particles encircled in the respective color of their AFM-IR spectrum (H) (magenta = salt, grey = soot, cyan = PS).

topographic and chemical images at 1100 cm^{-1} (Fig. 7D and S14B). Externally mixed PS and soot agglomerates were identified by specific chemical maps and were confirmed by recording full AFM-IR spectra (Fig. 7H). Complementary SEM–EDX analysis of this atmospheric aerosol sample (sample 17) confirmed the even deposition of the particles on the Si-wafer (Fig. S15). In addition to PS, soot and mineral dust particles, an iron oxide particle was additionally identified. Furthermore, a particle containing nitrogen (possibly protein/dead skin) was identified through EDX analysis (Fig. S16).

The composition of the ambient aerosol (sample 17) was dominated by sulfate, soot-like carbonaceous material, and mineral dust, consistent with previous observations.[51] Although organic aerosol is abundant in the atmosphere,[51] it was not identified here. Possibly, the particles classified as soot contained some or even predominantly oxidized organic compounds (secondary organic aerosol). Therefore, this class should be interpreted broadly as carbonaceous particles comprising both elemental and organic carbon.

The overwhelming dominance of sulfate droplets (Fig. 7) in ambient aerosol samples compromised the measurements due to frequent AFM tip contamination leading to imaging and spectral artifacts. To reduce these effects, sulfate was selectively removed by depositing a droplet of ultrapure water onto the Si-wafer for one minute, followed by blowing off the droplet containing the dissolved salts with pressurized nitrogen. Images recoded after the cleaning procedure demonstrated that PS and soot particles remained attached to the Si-wafer (Fig. S17). We assume that the interactions between the 200 nm PS and the Si-wafer are dominated by van der Waals forces whereas electrical forces related to the interactions between the polar Si (or rather the native oxide layer) and the non-polar PS are negligible. Due to the minimal contact area between spherical particles and the flat Si-wafer, we further expect the least interaction forces between 200 nm PS particles and the Si-wafer. Based on the good correspondence between the images of our (PS) spiked samples recorded before and after the washing step, we concluded that particle losses were of minor importance. However, we are aware that some particles may have been lost during the washing step.

3.5.2. Measurement of atmospheric particles after removal of sulfate. Based on the promising results we obtained from our sample-cleaning approach (insoluble components remained attached to the Si-wafer), an additional ambient aerosol sample (sample 18) was collected, cleaned as described above, and investigated using AFM-IR (Fig. 8). A total of 14 data cubes were acquired, whereas each data cube consisted of a topography (Fig. 8A) and a phase (Fig. 8B) image of a 10 × 10 μm^2 area and corresponding chemical maps recorded at wavenumbers of

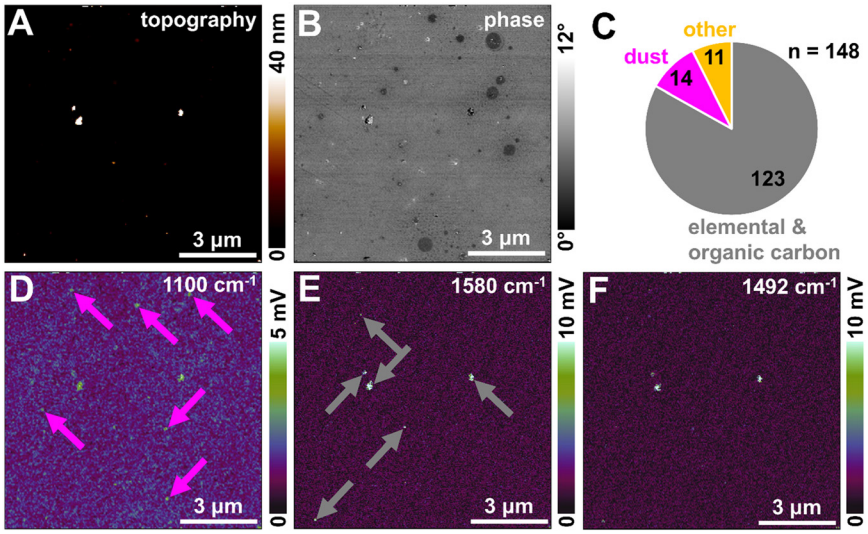

Fig. 8 Atomic force microscopy (AFM) (A) topography, (B) phase and (D–F) infrared (IR) amplitude images of an ambient aerosol sample after removal of soluble salts (sample 18). Silicate (magenta arrows) and elemental and organic carbon particles (grey arrows) were identified through the IR amplitude maps at 1100 (D) and 1580 cm^{-1} (E), respectively. At 1492 cm^{-1} (F), only carbonaceous particles showed an IR absorption signal. (C) Total number of particles detected based on 14 data cubes.

1100, 1492, and 1580 cm^{-1} (Fig. 8D–F). The wavenumbers were selected to allow the identification of major aerosol compounds (elemental and organic carbon, mineral dust) and NPs (PS). Fig. 8 shows an exemplary dataset, with silicate and elemental and organic carbon particles indicated by magenta (Fig. 8D) and grey (Fig. 8E) arrows, respectively. Additional chemical images were recorded at 1460 cm^{-1} for the detection of C–H bending vibrations of PE and PP methylene groups, and at 1730 cm^{-1} for identifying C=O stretching vibrations of PMMA and polyester (PET) ester groups (Fig. S18). In total, 148 particles were analyzed. Among them, 123 were identified as elemental and organic carbon, 14 as silicate dust. Eleven particles remained unclassified (Fig. 8C). However, based on the chemical maps, we can rule out that these particles represent conventional polymers (*e.g.*, PE, PP, PS, PMMA, PET). One particle likely consisted of epithelial keratin, a major proteinaceous component of household dust (Fig. S19),[52] which was identified with AFM-IR before in indoor aerosols.[37]

After the removal of the soluble sulfate salts as described above, elemental and organic carbon particles clearly dominated the detected particles. Based on the absence of NP within our dataset, the maximum NPs concentration in ambient air at the location and time of sampling was estimated based on the following reasoning. We would like to point out that although our statistical assessment is methodologically sound, it is based on a single sample collected at one location and time. Moreover, our analysis assumes that the sample represents the ambient aerosol and that further processing steps did not introduce any bias. Accordingly, the results should be interpreted primarily as providing contextualization of estimated NP concentrations relative to total particle number concentrations observed in ambient air.

From the total collected air volume (240 min at 0.5 L min^{-1} flow rate = 120 000 cm^3), 1.5%[43] of the particles in the collected air volume were electrostatically deposited randomly and size-independently on the Si-wafer and were therefore representative for a volume of 1800 cm^3. The area probed by AFM-IR in the 14 subsampled data cubes (10 × 10 μm^2 each) corresponded to 0.022% of the total area (circle with a diameter of 3 mm), resulting in a total probed air volume of 0.4 cm^3. The analysis of all particles in the subsampled area can be regarded as a random draw of particles from the air sample, representative of the location and time of sampling. Statistically, this situation corresponds to a binomial trial with two possible outcomes per draw: success, if the particle is a NP, or failure, if not. In this experiment, 148 independent trials were conducted without a single success. To estimate the range of NP proportions compatible with this outcome, an exact 95% confidence interval was calculated using the function *binom.confint* in the library *binom*[53] of R.[54] For n = 148 and x = 0 detections, the resulting interval was [0, 0.0246] and thus, the upper 95% confidence limit for the true fraction of NP among all particles was 2.46%. This corresponds to approximately 3.6 NPs that could have been present among the 148 analyzed particles, assuming the upper boundary of the confidence interval was valid. Given that these 148 particles represent an air volume of 0.4 cm^3, the corresponding upper-limit concentration is 9.1 NPs per cm^3.

This number can be converted into a theoretical upper-limit NP mass concentration assuming monodisperse spherical NP particles with a diameter of 100 nm and a density of 1 g cm^{-3}, resulting in a maximal mass concentration of 9.5 ng m^{-3}. We would like to emphasize that the values calculated above represent the statistical upper bound of NP concentration and since the sample size was rather small and no NP were detected, this remains a rough estimate for the upper limit rather than a measured concentration. The considerable uncertainty arises

from both the limited number of analyzed particles (low n) and the complete absence of detected NPs ($x = 0$). Increasing the number of analyzed particles would reduce the confidence interval width, however, AFM-IR is a low-throughput technique, and only a few hundred particles can realistically be analyzed within a reasonable timeframe. Typical concentrations of atmospheric nanoparticles next to a busy road are around 10 000 particles cm^{-3}.[55] Thus, given the limited throughput of our (particle-based) AFM-IR approach, NPs would need to be enriched by at least two orders of magnitudes, to allow for a statistically meaningful detection of atmospheric NPs. In other words, at least 99% of the (nano)particles from the ambient air would have to be eliminated. However, separating NPs from other nanoscale aerosols present in the atmosphere will be challenging, as their size and aerodynamic behavior are similar. Nevertheless, cascade impactors may offer a promising alternative sampling approach, as these instruments allow selecting different size fractions (*e.g.* 100–500 nm) at which the NP-background ratios may be higher.

4. Conclusion

This study systematically evaluated the possibilities and limitations of AFM-IR for detecting and chemically identifying nanoparticles in ambient aerosols, with a focus on nanoplastic particles (NPs). We established a complete analytical workflow that includes substrate selection, particle deposition and nanoscale spectral analysis. Silicon-wafers were identified as the most suitable substrate because they provide a low infrared background and are compatible with electrostatic precipitation. The minimum detectable particle sizes were 20 nm for silica, 80 nm for PS, 100 nm for PMMA and 200 nm for PE, showing that AFM-IR can achieve nanoscale chemical resolution for a range of particle types. Nanoparticles from synthetic aerosols were successfully collected by electrostatic precipitation, and AFM-IR analysis allowed the identification of different particle types. Most relevant (nano)particles in ambient air, including aged soot, mineral dust and sulfate salts, were clearly distinguished from model NPs based on characteristic infrared absorption bands. After removal of (soluble) sulfate precipitates from ambient air samples, the remaining nanoparticles were dominated by elemental and organic carbon particles (most likely mixtures of soot and secondary organic aerosols).

The nanoscale spatial resolution and chemical specificity allows for an unambiguous identification of NPs in complex matrices, as demonstrated for ambient air samples using PS spiked substrates. However, the limited sample throughput of AFM-IR combined with the low abundance of NPs relative to other atmospheric nanoparticles, such as soot, make the NP detection in ambient air samples very challenging. Nevertheless, based on a statistical evaluation of our AFM-IR data, essentially derived from the absence of NPs in our experimental dataset collected from ambient air samples, we anticipate that an enrichment of NPs of at least 2 orders of magnitudes is required for a reliable detection of NP by AFM-IR. Still, the AFM-IR method holds great potential in applications where NPs represent major components, *e.g.*, characterizing new NP reference materials. Further progress in enrichment of NPs from complex matrices is, however, urgently needed, before AFM-IR approaches can unfold their full potential.

Author contributions

N. K., C. H. and R. K. conceived the project. N. K., S. H., T. K. and R. K. performed the experiments. N. K., S. H., T. K. and R. K. analyzed the data. K. V., C. H. and R. K. supervised the project and provided conceptual advice. N. K. and R. K. wrote the article. S. H., T. K., K. V. and C. H. contributed to the critical revision and refinement of the manuscript.

Conflicts of interest

The authors declare that they have no known competing financial interests or personal relationships that could have appeared to influence the work reported in this paper.

Data availability

All data needed to evaluate the conclusions of the paper are present in the paper and the supplementary information (SI) file. Other data are available from the corresponding authors upon request.

Supplementary information is available. See DOI: https://doi.org/10.1039/d5en01155h.

Acknowledgements

N. K. and R. K. gratefully acknowledge the BNF program of the University of Bern for their administrative assistance and financial support for consumables. The authors thank Dr. Michele Griffa from the Concrete and Asphalt Laboratory at Empa for granting access to the AFM-IR system, and Dr. Peter Nirmalraj from the Transport at Nanoscale Interfaces Laboratory at Empa for providing AFM-IR probes. The authors also thank Jacqueline Tschudin from the Functional Polymers Laboratory at Empa for granting access to the FTIR spectrometer.

References

1 R. C. Thompson, W. Courtene-Jones, J. Boucher, S. Pahl, K. Raubenheimer and A. A. Koelmans, *Science*, 2024, **0**, eadl2746.
2 D. M. Mitrano, P. Wick and B. Nowack, *Nat. Nanotechnol.*, 2021, **16**, 491–500.
3 H.-C. Kung, C.-H. Wu, N. K. Cheruiyot, J. K. Mutuku, B.-W. Huang and G.-P. Chang-Chien, *Aerosol Air Qual. Res.*, 2023, **23**, 220362.

4 B. Giechaskiel, T. Grigoratos, M. Mathissen, J. Quik, P. Tromp, M. Gustafsson, V. Franco and P. Dilara, *Sustainability*, 2024, **16**, 522.
5 S. Allen, D. Allen, V. R. Phoenix, G. Le Roux, P. Durántez Jiménez, A. Simonneau, S. Binet and D. Galop, *Nat. Geosci.*, 2019, **12**, 339–344.
6 D. Allen, S. Allen, S. Abbasi, A. Baker, M. Bergmann, J. Brahney, T. Butler, R. A. Duce, S. Eckhardt, N. Evangeliou, T. Jickells, M. Kanakidou, P. Kershaw, P. Laj, J. Levermore, D. Li, P. Liss, K. Liu, N. Mahowald, P. Masque, D. Materić, A. G. Mayes, P. McGinnity, I. Osvath, K. A. Prather, J. M. Prospero, L. E. Revell, S. G. Sander, W. J. Shim, J. Slade, A. Stein, O. Tarasova and S. Wright, *Nat. Rev. Earth Environ.*, 2022, **3**, 393–405.
7 M. Aeschlimann, G. Li, Z. A. Kanji and D. M. Mitrano, *Nat. Geosci.*, 2022, **15**, 967–975.
8 N. Evangeliou, H. Grythe, Z. Klimont, C. Heyes, S. Eckhardt, S. Lopez-Aparicio and A. Stohl, *Nat. Commun.*, 2020, **11**, 3381.
9 A. Choudhury, F. Z. Simnani, D. Singh, P. Patel, A. Sinha, A. Nandi, A. Ghosh, U. Saha, K. Kumari, S. K. Jaganathan, N. K. Kaushik, P. K. Panda, M. Suar and S. K. Verma, *Ecotoxicol. Environ. Saf.*, 2023, **259**, 115018.
10 A. J. Nihart, M. A. Garcia, E. El Hayek, R. Liu, M. Olewine, J. D. Kingston, E. F. Castillo, R. R. Gullapalli, T. Howard, B. Bleske, J. Scott, J. Gonzalez-Estrella, J. M. Gross, M. Spilde, N. L. Adolphi, D. F. Gallego, H. S. Jarrell, G. Dvorscak, M. E. Zuluaga-Ruiz, A. B. West and M. J. Campen, *Nat. Med.*, 2025, **31**, 1114–1119.
11 S. Primpke, S. H. Christiansen, W. Cowger, H. De Frond, A. Deshpande, M. Fischer, E. B. Holland, M. Meyns, B. A. O'Donnell, B. E. Ossmann, M. Pittroff, G. Sarau, B. M. Scholz-Böttcher and K. J. Wiggin, *Appl. Spectrosc.*, 2020, **74**, 1012–1047.
12 N. P. Ivleva, *Chem. Rev.*, 2021, **121**, 11886–11936.
13 J. Xie, A. Gowen, W. Xu and J. Xu, *Anal. Methods*, 2024, **16**, 2177–2197.
14 N. B. Hartmann, T. Hüffer, R. C. Thompson, M. Hassellöv, A. Verschoor, A. E. Daugaard, S. Rist, T. Karlsson, N. Brennholt, M. Cole, M. P. Herrling, M. C. Hess, N. P. Ivleva, A. L. Lusher and M. Wagner, *Environ. Sci. Technol.*, 2019, **53**, 1039–1047.
15 M. E. Seeley and J. M. Lynch, *Anal. Bioanal. Chem.*, 2023, **415**, 2873–2890.
16 R. Kaegi, M. Philipp, I. S. Jüngling, N. P. Ivleva and T. D. Bucheli, *Anal. Bioanal. Chem.*, 2025, **417**, 6191–6208.
17 M. Dendisová, A. Jeništová, A. Parchaňská-Kokaislová, P. Matějka, V. Prokopec and M. Švecová, *Anal. Chim. Acta*, 2018, **1031**, 1–14.
18 D. Kurouski, A. Dazzi, R. Zenobi and A. Centrone, *Chem. Soc. Rev.*, 2020, **49**, 3315–3347.
19 Q. Xie and X. G. Xu, *Langmuir*, 2023, **39**, 17593–17599.
20 J. Shen, B.-I. Noh, P. Chen and S. Dai, *Small Sci.*, 2024, **4**, 2400297.
21 A. Dazzi, R. Prazeres, F. Glotin and J. M. Ortega, *Opt. Lett.*, 2005, **30**, 2388–2390.
22 A. Dazzi, C. B. Prater, Q. Hu, D. B. Chase, J. F. Rabolt and C. Marcott, *Appl. Spectrosc.*, 2012, **66**, 1365–1384.
23 L. D. B. Mandemaker and F. Meirer, *Angew. Chem., Int. Ed.*, 2023, **62**, e202210494.
24 H. Luo, Y. Xiang, Y. Zhao, Y. Li and X. Pan, *Sci. Total Environ.*, 2020, **744**, 140944.
25 H. Luo, Y. Xiang, Y. Li, Y. Zhao and X. Pan, *J. Hazard. Mater.*, 2021, **404**, 124159.
26 H. Luo, Y. Zeng, Y. Zhao, Y. Xiang, Y. Li and X. Pan, *J. Hazard. Mater.*, 2021, **413**, 125342.
27 H. Luo, C. Tu, C. Liu, Y. Zeng, D. He, A. Zhang, J. Xu and X. Pan, *Sci. Total Environ.*, 2024, **920**, 170933.
28 R. L. Merzel, L. Purser, T. L. Soucy, M. Olszewski, I. Colón-Bernal, M. Duhaime, A. K. Elgin and M. M. Banaszak Holl, *Glob. Chall.*, 2020, **4**, 1800104.
29 I. C. ten Have, A. J. A. Duijndam, R. Oord, H. J. M. van Berlo-van den Broek, I. Vollmer, B. M. Weckhuysen and F. Meirer, *Chem.: Methods*, 2021, **1**, 205–209.
30 M. Meyns, F. Dietz, C.-S. Weinhold, H. Züge, S. Finckh and G. Gerdts, *Anal. Methods*, 2023, **15**, 606–617.
31 Y. Li, Z. Wang and B. Guan, *Environ. Res.*, 2022, **204**, 112134.
32 Y. Li, C. Zhang, Z. Tian, X. Cai and B. Guan, *J. Hazard. Mater.*, 2024, **463**, 132933.
33 F. Ruggeri, C. Vitali, M. M. W. Nielen, H.-G. Janssen and A. K. Undas, *Research Square*, 2025, DOI: 10.21203/rs.3.rs-6719488/v1.
34 D. Khanal, J. Zhang, W.-R. Ke, M. M. Banaszak Holl and H.-K. Chan, *Anal. Chem.*, 2020, **92**, 8323–8332.
35 J. Zhang, D. Khanal, H.-K. Chan and M. M. Banaszak Holl, *Int. J. Pharm.*, 2024, **656**, 124116.
36 A. L. Bondy, R. M. Kirpes, R. L. Merzel, K. A. Pratt, M. M. Banaszak Holl and A. P. Ault, *Anal. Chem.*, 2017, **89**, 8594–8598.
37 J. M. González-Fialkowski, L. Wang, Y. Li and X. G. Xu, *Anal. Chem.*, 2021, **93**, 16845–16852.
38 S. Rizevsky, K. Zhaliazka, T. Dou, M. Matveyenka and D. Kurouski, *J. Phys. Chem. C*, 2022, **126**, 4157–4162.
39 S. Horender, K. Auderset, P. Quincey, S. Seeger, S. N. Skov, K. Dirscherl, T. O. M. Smith, K. Williams, C. C. Aegerter, D. M. Kalbermatter, F. Gaie-Levrel and K. Vasilatou, *Atmos. Meas. Tech.*, 2021, **14**, 1225–1238.
40 M. N. Ess, M. Bertò, A. Keller, M. Gysel-Beer and K. Vasilatou, *J. Aerosol Sci.*, 2021, **157**, 105820.
41 S. Horender, G. Tancev, K. Auderset and K. Vasilatou, *Appl. Sci.*, 2021, **11**, 9014.
42 D. Y. H. Pui, S. Fruin and P. H. McMurry, *Aerosol Sci. Technol.*, 1988, **8**, 173–187.
43 R. Kaegi, M. Fierz and B. Hattendorf, *Microsc. Microanal. Off. J. Microsc. Soc. Am. Microbeam Anal. Soc. Microsc. Soc. Can.*, 2021, 1–9.
44 A. Dazzi and C. B. Prater, *Chem. Rev.*, 2017, **117**, 5146–5173.
45 L. Quaroni, *Anal. Chem.*, 2020, **92**, 3544–3554.
46 M. R. Jung, F. D. Horgen, S. V. Orski, V. Rodriguez C., K. L. Beers, G. H. Balazs, T. T. Jones, T. M. Work, K. C. Brignac, S.-J. Royer, K. D. Hyrenbach, B. A. Jensen and J. M. Lynch, *Mar. Pollut. Bull.*, 2018, **127**, 704–716.

47 T. de los Arcos, H. Müller, F. Wang, V. R. Damerla, C. Hoppe, C. Weinberger, M. Tiemann and G. Grundmeier, *Vib. Spectrosc.*, 2021, **114**, 103256.
48 M. Della Ciana, A. Kovtun, C. Summonte, A. Candini, D. Cavalcoli, D. Gentili, R. Nipoti and C. Albonetti, *Langmuir*, 2023, **39**, 12430–12451.
49 J. R. Keifer, M. Novicky, M. S. Akhter, A. R. Chughtai and D. M. Smith, in 1981 Intl Conf on Fourier Transform Infrared Spectroscopy, SPIE, 1981, vol. 0289, pp. 184–188.
50 V. Goel, S. K. Mishra, C. Sharma, B. Sarangi, S. G. Aggarwal, R. Agnihotri and R. K. Kotnala, *MAPAN*, 2018, **33**, 209–215.
51 S. K. Grange, A. Fischer, C. Zellweger, A. Alastuey, X. Querol, J.-L. Jaffrezo, S. Weber, G. Uzu and C. Hueglin, *Atmos. Environ.:X*, 2021, **12**, 100145.
52 K. Fox, E. Castanha, A. Fox, C. Feigley and D. Salzberg, *J. Environ. Monit.*, 2008, **10**, 55–59.
53 S. Dorai-Raj, binom (version 1.1–1.1), https://cran.r-project.org/web/packages/binom/index.html, 2022.
54 R Core Team, R Core Team. (2025) R A Language and Environment for Statistical Computing, R Foundation for Statistical Computing. - References - Scientific Research Publishing, https://www.scirp.org/reference/referencespapers?referenceid=3967248, (accessed February 6, 2026).
55 P. Trechera, M. Garcia-Marlès, X. Liu, C. Reche, N. Pérez, M. Savadkoohi, D. Beddows, I. Salma, M. Vörösmarty, A. Casans, J. A. Casquero-Vera, C. Hueglin, N. Marchand, B. Chazeau, G. Gille, P. Kalkavouras, N. Mihalopoulos, J. Ondracek, N. Zikova, J. V. Niemi, H. E. Manninen, D. C. Green, A. H. Tremper, M. Norman, S. Vratolis, K. Eleftheriadis, F. J. Gómez-Moreno, E. Alonso-Blanco, H. Gerwig, A. Wiedensohler, K. Weinhold, M. Merkel, S. Bastian, J.-E. Petit, O. Favez, S. Crumeyrolle, N. Ferlay, S. Martins Dos Santos, J.-P. Putaud, H. Timonen, J. Lampilahti, C. Asbach, C. Wolf, H. Kaminski, H. Altug, B. Hoffmann, D. Q. Rich, M. Pandolfi, R. M. Harrison, P. K. Hopke, T. Petäjä, A. Alastuey and X. Querol, *Environ. Int.*, 2023, **172**, 107744.